TURBULENCE MEASUREMENTS DOWNSTREAM OF A COMBUSTOR SIMULATOR DESIGNED FOR STUDIES ON THE COMBUSTOR-TURBINE INTERACTION

A. Notaristefano - G. Persico – P. Gaetani

Address: Department of Energy, Politecnico di Milano, Milano, Italy,
andrea.notaristefano@polimi.it, giacomo.persico@polimi.it, paolo.gaetani@polimi.it

ABSTRACT

Turbulence intensity impacts the performance of turbine stages and is an important inlet boundary condition for CFD computations; the knowledge of its value at the turbine inlet is then of paramount importance.

In combustor–turbine interaction experimental studies, combustor simulators replace real combustors and allow the introduction of flow perturbation at the turbine inlet. Therefore, the turbulence intensity of a combustor simulator used in a wide experimental campaign at Politecnico di Milano is characterized by means of a hot-wire probe in a blow-down wind tunnel and the results are compared to URANS CFD computations. This combustor simulator can generate a combination of a swirl profile with a steady/unsteady temperature disturbance. In the cold unsteady disturbance case, hot-wire measurements are phase-averaged at the frequency of the injected perturbation. The combustor simulator turbulence intensity is measured at two different axial positions to understand its evolution.

KEYWORDS

COMBUSTOR-TURBINE INTERACTION, TURBULENCE, HOT-WIRE, MEASURING TECHNIQUES

NOMENCLATURE

A, B, n	King's coefficients	p	Pressure
A_i	Coefficients Eq. (9)	Q	Cooling velocity
c	Chord	q	Fluctuating cooling velocity
CS	Cold streak	r, Θ, z	Coordinates of polar reference system
d	Diameter		
E	Voltage supply	R	Coefficients of Eq. (11)
e	Fluctuating voltage supply	Re	Reynolds number
EW	Entropy wave	S	Surface
HS	Hot streak	SN	Swirl number
HW	Hot wire	T	Temperature
k^2, h^2	Jorgensen's calibration coeff.	Ti	Turbulence intensity
LE	Leading edge	U	Velocity
$\hat{n}$	Unit vector normal to S	u	Fluctuating velocity
M	Mach number	x, y, z	ref. system coordinates
MS	Mainstream	Z	Coefficients of Eq. (13)

α	Hot-wire slanted angle
θ	Pitch angle
λ	Integral length scale
φ	Yaw angle

Subscripts

0	Rest condition
1, 2, 3	Components on y, z, x
corr	After temperature correction
n, t, b	Hot-wire reference system
rot	Motor rotation
t	Total
w	Wire
Θ	Tangential component

INTRODUCTION

To reduce pollutant emissions of gas turbines for both propulsive and stationary applications combustors are designed to burn a lean-premixed mixture. In addition, a strong swirl is imposed on the combustion air to enhance air-fuel mixing and stabilize the flame. Lean burn combustors release a flow field characterized by unsteady temperature and velocity inhomogeneities both in radial and circumferential directions. Especially in aeroengines, where compactness is required, such non homogeneities move downstream until the first turbine stage and, notwithstanding an attenuation in the combustor duct, they impact the blade aerodynamics, the blade cooling effectiveness (Gundy-Burlet and Dorney (1997)) and combustion noise (Morgans and Duran (2016)).

As such impact cannot be neglected, several experimental and numerical investigations were performed to identify, describe and quantify it, with the aim of improving the control of the combustor-turbine interaction (Khanal et al. (2013), Rahim and He (2015), Andreini et al. (2016), Werschnik et al. (2017), Adams et al. (2021), Mansouri and Jefferson-Loveday (2022), Notaristefano and Gaetani (2023a) and Notaristefano and Gaetani (2023b)).

In this context, many combustor simulators (used by Andreini et al. (2016), Werschnik et al. (2017), Notaristefano and Gaetani (2020) and Adams et al. (2021)) were conceived to mimic, by non-reactive devices, the combustor released flow and to allow the experimental testing and numerical simulation.

As demonstrated by Khanal et al. (2013), to consider individually the combustor non-uniformities is questionable because the nonlinearity of the process prevents a straightforward superposition of the effects. In addition to these features, the unsteadiness of the temperature pattern makes the study much more complex and requires dedicated combustor simulator for running experiments. As a matter of fact, nowadays there is a growing interest in studying the combined injection of a swirl profile and hot-streaks / entropy waves (Khanal et al. (2013), Rahim and He (2015), Andreini et al. (2016), Werschnik et al. (2017), Adams et al. (2021), Mansouri and Jefferson-Loveday (2022) and Notaristefano and Gaetani (2022)). Several experimental campaigns have been performed at Politecnico di Milano since 2015 (Gaetani and Persico, 2019), focused on the transport of entropy waves within a HP turbine stage. The most recent combustor simulator used to generate the turbine-inlet non-uniformities was conceived to combine a swirl profile and entropy waves (Notaristefano and Gaetani (2020)): such an inlet flow field makes this experimental campaign one of a kind. The results of this wide experimental campaign are described in Notaristefano and Gaetani (2023a), Notaristefano and Gaetani (2023b) and Pinelli et al. (2023), the interested reader is invited to refer to them for detailed results.

In those papers the information about the turbulence of the flow at the turbine inlet was missing due to the mechanical constraints of the turbine rig that did not allow to insert a hot wire, commonly considered as the primary tool for such kind of measurements. As found by previous authors (Folk et al. (2020), Bons (2002), Thole and Bogard (1995)), turbulence intensity impacts the turbine loss mechanisms and increase the heat transfer. Therefore, this is an important feature that has to be

reproduced by combustor simulators. In fact, combustor outlet turbulence can exceed the 10 % (Zimmerman (1979), Seasholtz et al.(1983), Cha et al.(2012)), which is a much higher value than can be achieved using grids. In Folk and Miller (2019), Cresci et al. (2015), and Bacci et al. (2015) the turbulence intensity generated by combustor simulators is studied. This paper aims at describing the turbulence field released by the combustor simulator described in Notaristefano and Gaetani (2020) and its decay as the stream propagates downstream. Experiments were performed at different injection conditions and at different distances from the injector. In addition, RANS CFD simulations were carried out to support the physical interpretation and to integrate the results of the experimental campaign.

CASE STUDY AND METHODS

To investigate the turbulence generated by the combustor simulator used on the turbine test rig at Politecnico di Milano, the simulator is placed in a blow-down wind tunnel that can replicate turbine inlet conditions by imposing the same Mach number. However, due to density effects, Reynolds number is 30% lower in this setup. Table 1 provides information regarding the mainstream properties. Considering the different flow features, three Re numbers are given: Re_{duct} is computed on the duct size, $Re_{c,swirler}$ is based on the chord of the swirler generator blades and $Re_{d,injecotor}$ is computed on the injector diameter. The calibrated nozzle of the wind tunnel is fed by compressed stocked air and has a square exit section of 0.08 m side. According to the nozzle calibration (Persico et al. (2010))), the open jet generated retains a wall-bounded character for an axial distance of two jet widths downstream of the nozzle. The combustor simulator is placed within a straight prolongation added downstream of the exit section (Fig. 1). This device includes a swirler generator, highlighted with a circle in Fig. 1, and can inject steady/unsteady temperature disturbances. Probes are traversed downstream of the device at two traversing planes, one representative of the plane where measurements are carried out upstream of the turbine stage, that is approximately one chord of the swirl generator blade downstream of the device itself, and the second at a position coincident with the turbine vane LE (in the turbine experiments). Both the planes are inside the axial extension of 2 jet widths. The characterization of the turbulence generated by the combustor simulator is carried out by means of a slanted hot-wire probe. In addition, a 5-hole probe is used to assess the hot-wire measurements.

Generated combustor disturbances

The combustor simulator allows for studying several steady/unsteady injection cases. In the steady cases, a by-pass valve is opened and only one duct, labelled “duct 1” in Fig. 1, is continuously fed. To simulate this condition in CFD, the inlet plane of duct 2 is treated as a wall. In the unsteady ones, a set of automotive valves are used to feed alternatively the two different ducts that are then rejoined at the head of the injector (Fig. 1). The air flowing in duct 1 can be heated up by an electric

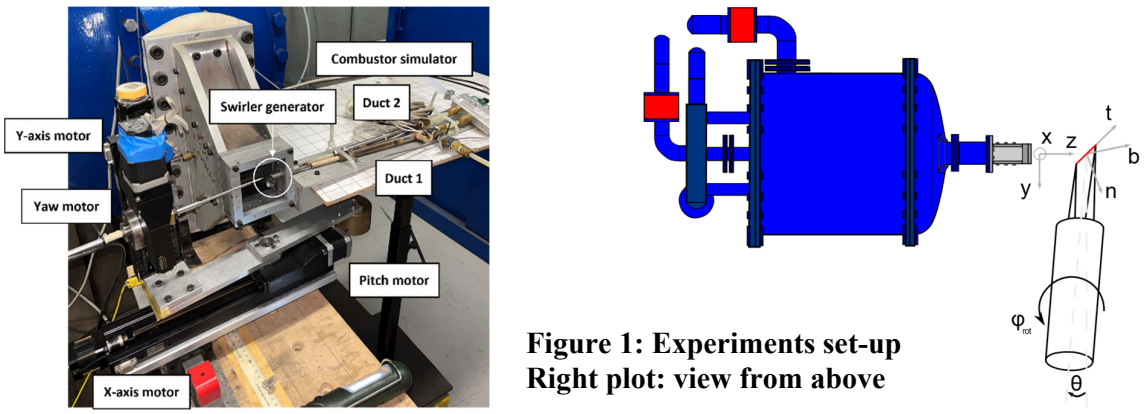

Figure 1: Experiments set-up
Right plot: view from above

heater. At the outlet of the injector, a swirl generator is placed that acts on both the mainstream air and the steady/unsteady generated disturbances. Further details of the combustor simulator are described in Notaristefano and Gaetani (2020).

Flows at ambient temperature are necessary for the hot-wire measurements because temperature affects the hot-wire calibration and a too high temperature can burn the wire. As such, the combustor simulator electric heater is switched off and hot cases are only simulated by means of CFD. Table 1 lists and defines the four injection cases studied. The first case, hot-streak (HS), involves a steady injection of hot flow into injector duct 1. In the second case, referred to as cold-streak (CS), the duct 1 is fed with a steady flow at ambient temperature. The third case, entropy wave (EW), features an alternate injection of hot and cold flows in ducts 1 and 2, respectively. Lastly, in the unsteady CS, ducts 1 and 2 are fed alternatively as in EW case, but the flow in duct 1 is at ambient temperature. The feeding pressure of the injector ducts used in turbine tests (Notaristefano and Gaetani (2023a)) is rescaled on the basis of the different pressure ratios.

Table 1: Injection cases and mainstream properties

		Duct 1			Duct 2				
Injection case name	Frequency [Hz]	Feed ?	CFD inlet plane treatment	T_t [K]	Feed ?	CFD inlet plane treatment	T_t [K]	Exp.	CFD
HS	0	No	Wall		Yes	Inlet	670		✓
CS	0	No	Wall		Yes	Inlet	303	✓	✓
EW	110	Yes	Inlet	303	Yes	Inlet	670		✓
Unsteady CS	110	Yes	Inlet	303	Yes	Inlet	303	✓	✓

	Re_{duct}	$Re_{c,swirler}$	$Re_{d,injector}$	M	Tt [K]
Mainstream	2.35×10^5	3.5×10^4	3.8×10^4	0.13	303

CFD set-up

A dedicated fully-3D URANS computational model was developed in the ANSYS-Fluent framework, considering the injector of the combustor simulator immersed in the nozzle airflow. Figure 2 shows a schematic of the three inlets and outlet boundary conditions. The inlet boundary is placed at the nozzle outlet section. Two further inlet conditions are placed at the head of the injector where steady/unsteady boundary conditions are set. Inlet boundary conditions include temperature and velocity magnitude, while the static pressure is specified at the outlet. The injector surfaces are modelled as no-slip walls, and the domain four lateral surfaces, i.e. the lateral surfaces of the jet, are modelled as slip walls. According to measurements, at the inlet the turbulence intensity is assigned equal to 1 %, the turbulence length scale is also assigned at 10% of the relevant inlet boundary scale.

Unsteady RANS CFD simulations are carried out also in steady injection cases to simulate the vortex shedding downstream of the injector stem, that would play a significant role in the decay of the main properties of the perturbation generated by the simulator. After having performed a FFT on the instantaneous mass-flow average at the outlet section, the main periodicity of the problem was identified and the period was discretized into 40 time steps.

Figure 2 shows a cut of the unstructured 3D mesh. Two meshes were tested and the results of a grid-independence analysis are shown in Tab. 2. The two meshes feature the same boundary layer resolution, characterized by 20 layers and a $y^+ < 1$. The mesh is not further coarsened to accurately catch the mixing that occurs downstream of the injector. Among the two tested meshes, the one with 6 million cells is used, considering the small differences in the outcomes of the grid-independence

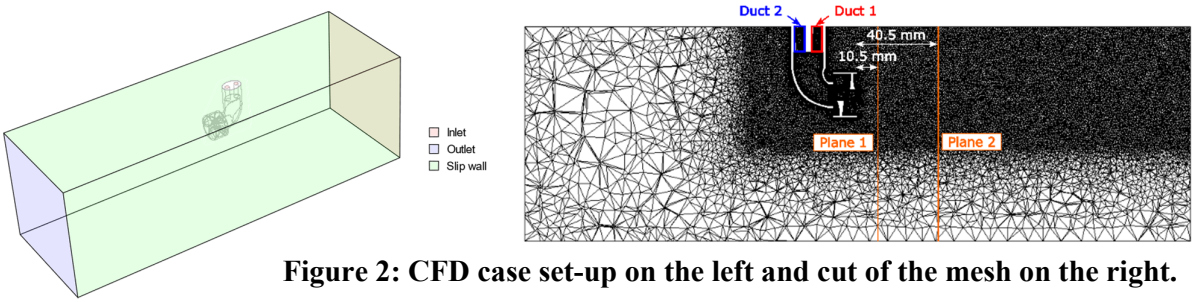

Figure 2: CFD case set-up on the left and cut of the mesh on the right.

analysis shown in Tab. 2.

Table 2: Grid independence analysis.

	Coarse	Fine	Δ
Number of cells	6 mln	12 mln	
$(P_{t_{inlet}} - P_{t_{outlet}})/(P_{t_{inlet}} - P_{s_{inlet}})$	0.038	0.034	0.49%
$T_{t_{outlet}} - T_{t_{inlet}}$ [K]	0.79	0.76	0.03

After several preliminary trials changing numerical schemes, the Fluent pressure-based coupled solver is selected, using the k-ω SST turbulence model and the ideal gas as a thermodynamic fluid model. High resolution in the numerical solution is achieved by adopting second-order upwind schemes for the advective fluxes, second-order central differences for the viscous terms, and the second-order implicit discretization of the unsteady term.

Measuring technique

This section describes the measurement techniques utilized during the experimental campaign. The pressure drop across the nozzle is measured by a Kulite™ XT190 transducer which has a full-scale of 5 psi. The outlet pressure is the ambient pressure which is read by a barometer Fisher™ model 104 with an average uncertainty of 50 Pa calibrated in the LAT n° 024. In order to phase-average the hot-wire measurements at the frequency of the injected disturbance, the pressure in the injector duct 1 is used as a trigger signal and is measured by means of a Kulite™ XT190 transducer with a full-scale of 25 psi. The transducers maximum uncertainty is 0.05 % of the transducer full scale. The measuring signals are acquired by means of a National Instrument data acquisition board (PCI 6052E) whose range is ±10 V.

Temperatures are measured by means of thermocouples: the nozzle supply air temperature is measured by a T-type, the injector ducts and ambient temperature by a K-type. Temperature uncertainty is 0.3°C.

At the traversing planes, a 5-hole probe and a hot-wire anemometer are used.

5-hole probe

A 5-hole pressure probe was used to characterize the steady aerodynamic flow field at the two traversing positions. The probe head has a diameter of 2.2 mm and an overhung of 5 mm.

The probe was aerodynamically calibrated in a Mach number range of 0.1 – 0.3 and in an angular range of ± 44° both in pitch and yaw angles, chosen to proficiently characterize the complex 3D field. The yaw angle is the angle around the probe axis, the pitch angle is the angle of inclination of the probe axis with respect to the main flow direction. The average uncertainties of the 5-hole probe were calculated using the Monte Carlo method described in Notaristefano et al. (2021) which predicts an average extended uncertainty of 1.5° for angles, 2.5 m/s for absolute velocity and 100 Pa for pressure.

Hot-wire

The hot-wire used in this experimental campaign is a slanted single-sensor probe, with a slanting angle of 45°, and connected to a DISA55M system. The wire diameter of ~5 µm guarantees a very high dynamic response (~30 kHz) in the constant temperature configuration, making this probe suitable to measure the turbulence structures of both low and high-speed flows. The probe is mounted on four stepping motors (Fig. 1): two of them control the traversing position, one controls the yaw angle and the last controls the pitch angle.

To keep the wire temperature constant in presence of an incoming flow, the hot-wire Wheatstone bridge regulates the supply voltage. This well-established response relationship is described by the King's law:

$$\bar{E}_{corr}^2 = A + BQ^n \tag{1}$$

Where $\bar{E}_{corr}$ is the mean average of the supply voltage, once corrected to account for temperature drifts, Q is the cooling velocity and A, B and n are calibration constants obtained after a least square regression of the calibration data. In King's law, the hot-wire is aligned perpendicularly to the main flow so that the cooling velocity Q corresponds to the flow velocity U. In the case of a slanted single-wire probe, this condition is respected placing the probe at a pitch angle of -45° and yaw angle of 0°. In such a way, the cooling velocity depends only on the normal component of the flow velocity and the other velocity components are null; in all other cases, one would need to know the angular sensitivity of the probe, which is normally still unknown at this stage of the calibration. Another constraint for determining King's law is that the turbulence intensity of the calibrating jet is small (below 5%) because, as it will be shown later, the velocity depends also on the Reynolds tensor components. Both these conditions were properly matched in the calibrations performed for this study.

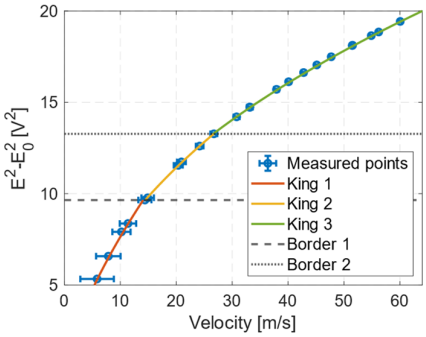

Figure 3: King's law.

The methodology applied in this work requires a careful discussion, as specific actions are taken to improve the results reliability. First, King's law is split into three different voltage ranges (Fig. 3) to improve the accuracy of the interpolation. Second, the anemometer output signal E is corrected to account for possible temperature drifts during the calibration using Eq. 2, suggested by Bruun (1995):

$$E_{corr}^2 = E^2 \frac{T_w - T_0}{T_w - T_{flow}} - E_0^2 \tag{2}$$

T_w is the constant temperature of the wire (set at 493 K), T_0 is the temperature at which the voltage zero E_0 is performed (at rest conditions) and T_{flow} is the temperature of the incoming air.

The fluctuating component of the cooling velocity is derived by decomposing King's law Perdichizzi et al. (1990). It depends on the King's coefficients and the mean velocity:

$$\overline{q^2} = \left[\frac{2\bar{E}_{corr}}{nB\bar{Q}^{n-1}}\right]^2 \overline{e^2} \tag{3}$$

Where q is the fluctuating velocity component and e is the root mean square of the hot-wire voltage measurements.

In real applications, the actual velocity could be not perpendicular to the wire. In this case, the other velocity components impact the cooling velocity of the hot-wire in a non-linear way. The influence of these velocity components on the cooling velocity is well-described by the Jorgensen's law (Perdichizzi et al. (1990)):

$$Q^2 = U_n^2 + k^2 U_t^2 + h^2 U_b^2 \tag{4}$$

Where n is the normal, t is the tangential and b is the binormal component with respect to the wire (Fig. 1). h^2 and k^2 are the two angular calibration coefficients to be defined through an aerodynamic calibration. It must be emphasized that in the definition of King's law only the normal component is not null; in fact, the change of reference system from the hot-wire to the nozzle one gives:

$$\begin{cases} U_n = U(cos\theta cos\varphi sin\alpha - sin\theta cos\alpha) \\ U_t = U(cos\theta cos\varphi cos\alpha + sin\theta sin\alpha) \\ U_b = -Ucos\theta sin\varphi \end{cases} \quad (5)$$

In the literature the coefficient k^2 is available for standard probes (Fitouri et al (1995)). In this paper application the choice is to carry out a calibration to determine also the k^2 coefficient varying the pitch angle. For this purpose, the hot-wire yaw angle is set to zero, that is U_b=0, and the pitch angle is varied on the calibration range of $\pm$ 45° every 5°. This is possible after having verified that the dependence of k^2 to the yaw angle is negligible. The k^2 can be computed accordingly to Eq. 6 imposing the yaw angle $\varphi = 0°$.

$$k^2 = \frac{\frac{Q^2}{U^2} - (cos\theta sin\alpha - sin\theta cos\alpha)}{cos\theta cos\alpha + sin\theta sin\alpha} \quad (6)$$

The last angular calibration coefficient h^2 can be calculated as shown in Eq. 7 imposing the different combinations of yaw and pitch angles. For each pitch angle, the yaw is moved in the range of $\pm$ 120° every 5°.

$$h^2 = \frac{\frac{Q^2}{U^2} - (cos\theta cos\varphi sin\alpha - sin\theta cos\alpha)^2 - k^2(cos\theta cos\varphi cos\alpha + sin\theta sin\alpha)^2}{(cos\theta sin\varphi)^2} \quad (7)$$

Once the calibration coefficients are defined, the probe can be applied in an unknown flow field to reconstruct its velocity components and the turbulence content. The flow velocity can be decomposed into its three components in the x-y-z reference system that can be correlated to the hot-wire reference system components by Eq. 8, where φ_{rot} is the rotation of the yaw motor.

$$\begin{cases} U_n = U_1 cos\alpha + U_2 cos\varphi_{rot} sin\alpha + U_3 sin\varphi_{rot} sin\alpha \\ U_t = -U_1 sin\alpha + U_2 cos\varphi_{rot} cos\alpha + U_3 sin\varphi_{rot} sin\alpha \\ U_b = U_2 sin\varphi_{rot} - U_3 cos\varphi_{rot} \end{cases} \quad (8)$$

Therefore, the cooling velocity can be related to the velocity components in the nozzle reference system replacing Eqs. 8 in Eq. 4:

$$Q^2 = A_{11}U_1^2 + A_{22}U_2^2 + A_{33}U_3^2 + A_{12}U_1U_2 + A_{23}U_2U_3 + A_{13}U_1U_3 \quad (9)$$

The coefficients A depend on the yaw angular position and the slanted angle, as well as the calibration coefficients h^2 and k^2. One single equation is not enough to solve the flow field, being the unknowns three. To obtain reliable results, the system is overdetermined using 13 equations, calculated by changing the probe yaw angle in the range $\pm$120° every 20°. This set of angles is chosen after a proper validation of the procedure considering different ranges and angle steps. The overdetermined problem is resolved using a Matlab iterative script and the *lsqnonlin* function. The first guess of the velocities is a vector of [0; Q; 0], with Q computed by King's law.

This procedure is valid in case of low turbulence intensity flows because the effective cooling velocity depends also on the fluctuating components. Expressing each velocity component in terms of mean (denoted with upper case letters) and fluctuating (denoted lower case letters) components, after calculating the mean value (denoted with an overline), Eq. 9 becomes:

$$\overline{Q^2} = A_{11}\left(\overline{U_1}^2 + \overline{u_1^2}\right) + A_{22}\left(\overline{U_2}^2 + \overline{u_2^2}\right) + A_{33}\left(\overline{U_3}^2 + \overline{u_3^2}\right) + A_{12}(\overline{U_1}\,\overline{U_2} + \overline{u_1u_2}) + A_{23}(\overline{U_2}\,\overline{U_3} + \overline{u_2u_3}) + A_{13}(\overline{U_1}\,\overline{U_3} + \overline{u_1u_3}) \quad (10)$$

This equation does not allow the separation of the time mean components and the Reynolds stresses. Equation 10 could be written in terms of both mean and Reynolds stress coefficients and considering the largest velocity component as the one in the axial direction (U_2):

$$Q = A_{22}^{\frac{1}{2}}\overline{U_2}\left\{\begin{array}{l}1+2\dfrac{u_2}{\overline{U_2}}+\left[\dfrac{u_2}{\overline{U_2}}\right]^2+\dfrac{A_{11}}{A_{22}}\left[\dfrac{\overline{U_1}+u_1}{\overline{U_2}}\right]^2+\dfrac{A_{33}}{A_{22}}\left[\dfrac{\overline{U_3}+u_3}{\overline{U_2}}\right]^2+\dfrac{A_{12}}{A_{22}}\left[1+\dfrac{u_2}{\overline{U_2}}\right] \\ \left[\dfrac{\overline{U_1}+u_1}{\overline{U_2}}\right]+\dfrac{A_{23}}{A_{22}}\left[1+\dfrac{u_2}{\overline{U_2}}\right]\left[\dfrac{\overline{U_3}+u_3}{\overline{U_2}}\right]+\dfrac{A_{13}}{A_{22}}\left[\dfrac{\overline{U_1}+u_1}{\overline{U_2}}\right]\left[\dfrac{\overline{U_3}+u_3}{\overline{U_2}}\right]\end{array}\right\}^{\frac{1}{2}} \quad (11)$$

After approximating at the first order the Eq. 11, the mean velocity and the mean of its fluctuating component can be derived. The hypothesis is that all the other components are much lower than $\overline{U_2}$, so that series expansion can be applied. Further neglecting third order terms or greater, according to Buresti and Di Cocco (1987) the mean effective velocity reads:

$$\bar{Q} = R_2\overline{U_2} + R_1\overline{U_1} + R_3\overline{U_3} + R_4\frac{\overline{U_1}^2}{\overline{U_2}} + R_5\frac{\overline{U_3}^2}{\overline{U_2}} + R_6\frac{\overline{U_1}\,\overline{U_3}}{\overline{U_2}} + R_4\frac{\overline{u_1}^2}{\overline{U_2}} + R_5\frac{\overline{u_3}^2}{\overline{U_2}} + R_6\frac{\overline{u_1}\,\overline{u_3}}{\overline{U_2}} \quad (12)$$

Considering that:

$$\overline{q^2} = \overline{Q^2} - \bar{Q}^2 \quad (13)$$

By subtracting Eq. 10 to Eq. 12, properly squared, and neglecting third-order terms:

$$\begin{aligned}\overline{q^2} = {} & Z_1\overline{u_2^2} + \left[Z_2 + 2Z_{10}\frac{\overline{U_1}}{\overline{U_2}} + Z_{12}\frac{\overline{U_3}}{\overline{U_2}}\right]\overline{u_1^2} + \left[Z_3 + Z_{13}\frac{\overline{U_1}}{\overline{U_2}} + 2Z_{15}\frac{\overline{U_3}}{\overline{U_2}}\right]\overline{u_3^2} + \\ & \left[Z_4 + 2Z_7\frac{\overline{U_1}}{\overline{U_2}} + 2Z_8\frac{\overline{U_3}}{\overline{U_2}}\right]\overline{u_1u_2} + \left[Z_5 + Z_8\frac{\overline{U_1}}{\overline{U_2}} + 2Z_9\frac{\overline{U_3}}{\overline{U_2}}\right]\overline{u_2u_3} + \\ & \left[Z_6 + Z_{11}\frac{\overline{U_1}}{\overline{U_2}} + Z_{14}\frac{\overline{U_3}}{\overline{U_2}}\right]\overline{u_1u_3}\end{aligned} \quad (14)$$

The use of these equations is justified by the fact that the turbulence intensity in this application does not exceed 20 % (Buresti and Di Cocco (1987)), making equations 12 and 14 consistent. In this way, all the components of the Reynolds stress tensor can be estimated.

All the coefficients (A Eq. 9, R Eq. 12 and Z Eq. 14) are taken from Buresti and Di Cocco (1987) and Fitouri et al. (1995), the only difference regards the different reference system.

However, at the first traversing position, the hypothesis of U_2 being the dominant velocity is not everywhere correct, especially in the vortex core. If the tangential velocity U_3 becomes dominant, this issue can be easily solved by rotating the reference system: after having estimated the velocity direction resolving the over-constrained system of equations, the central hot-wire rotation is updated to the actual velocity direction. In such a way, U_2 is again the main velocity component and previous equations can be applied. To make this possible, it is necessary to arrange measurements on a wider range of motor rotations to account for the possible change in the reference system. Therefore, for each point, measurements are carried out in a range $\pm 160°$, being $\pm 40°$ the maximum/minimum angles expected.

In the case the U_1 is the dominant component, previous equations are derived again changing the procedure from equation 11 on.

In the end the procedure to resolve the flow field with the hot-wire follows the next steps:

1. The acquired voltages are used to compute the $\bar{Q}$ and $\bar{q}$ by applying King's law.
2. Under the hypothesis of low turbulence content and Q=[0, $\bar{Q}$, 0], the mean flow field is solved by iterating on the Eq. 9 given 13 sets of rotations.
3. The first prediction of the velocity vector is used to update the rotational range and to solve the Reynolds tensor (Eq. 14). The updated rotational range is centered on the nearest multiple of 20° relative to the measured yaw angle, and it includes 13 rotations, spaced every 20° within the range of ±120° with respect to that closest multiple of 20°.
4. Considering that the mean velocity depends on the Reynolds stress tensor components (Eq.

10), the hypothesis done at step 2 is now relaxed resolving again the mean velocity components by means of a least square regression on Eq. 10, knowing the Reynolds stresses computed at step 3.

5. With the new mean velocities, the cycle is repeated starting from step 3 until convergence.

A Monte Carlo simulation has been carried out to perform an uncertainty quantification of the HW measurements. Starting from the measuring uncertainties, these are propagated through the whole calibration process. Uncertainties are different depending on the flow regime, considering the high uncertainties associated to low speed (see Fig. 3). The extended uncertainties at 95% confidence interval are listed in Tab. 3 for the flow quantities object of this study.

Table 3: HW uncertainties at 95% confidence interval.

	Mainstream	Perturbed region
Ti	0.07 %	5 %
U [m/s]	0.5	4.8
U_3 [m/s]	1	8
λ [m]	2.6×10^{-4}	8×10^{-5}

RESULTS

Steady cold-streak

The first analysis was focused on the validation of the CFD model on the CS case. The validation process involved the analysis of the spanwise profiles of horizontally mass-averaged quantities at the two traversing planes. The results of this comparison are shown in Fig. 4. The total pressure and the velocity are compared between CFD and 5-hole probe measurements, both made non-dimensional with respect to the undisturbed mainstream (MS) values. CFD effectively captured the evolution of the lower and upper branches of the swirl profile. The agreement becomes poorer in the stem wake region, especially at plane 1. The main potential cause for this discrepancy is that the CFD model does not reliably predict the streamwise evolution of the vortexes shed by the injector stem.

To better understand the spanwise profiles of Fig. 4, the contour plots from both experiments and CFD have been compared at the first traversing plane in terms of absolute velocity (Fig. 5), tangential velocity (Fig. 7) and turbulence intensity (Fig. 8). All these plots were generated with the perspective of an observer placed downstream of the studied plane. In the region of the swirl core at the first traversing plane, both the hot-wire and 5-hole probe operate near the angular boundaries of their calibration ranges, making some measurements affected by a higher error. Notwithstanding this problem, the agreement between measurements and CFD is good. Analyzing the results, two main flow structures are observed.The first one corresponds to the wake generated by the injector stem, which is highlighted with a white box in Fig. 5 CFD. The second one is the swirl profile, which is identified by a white circle. Comparing CFD results with experiments, the agreement is good in terms of velocity magnitude and flow morphology.

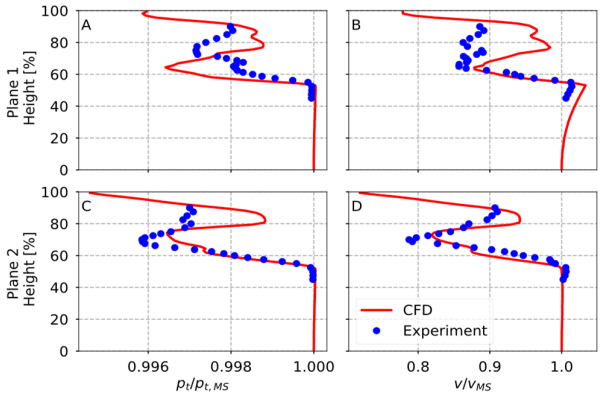

Figure 4: Y-axis mass average comparisons on total pressure and velocity.

Along the circumference of the swirl profile, three regions of high velocity magnitude are identified, numbered 3-4-5 in Fig. 5 CFD. These correspond to the flow released by the swirler generator vanes 3-4-5, as identified in the contour "Plane 0" that is the X-Y plane at the swirler generator trailing edge. The other swirler generator channels 1-2 exhibit a low velocity because they collect the flow from the injector stem wake. Furthermore, the injected cold streak

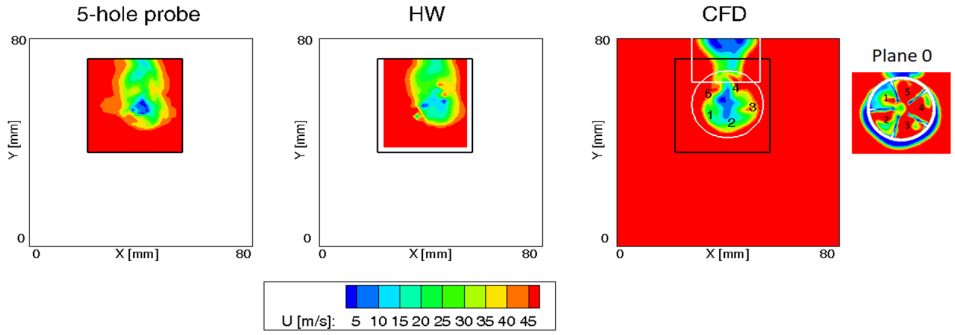

Figure 5: Absolute velocity contours at Plane1. Plane 0 refers to a plane at the swirler generator trailing edge. Numbers 1-5 rotates between the two planes as a consequence of the swirl components.

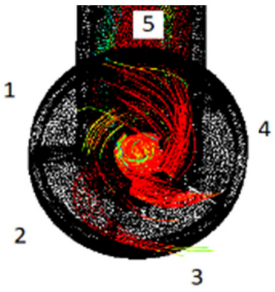

Figure 6: Streamlines of the injected disturbance.

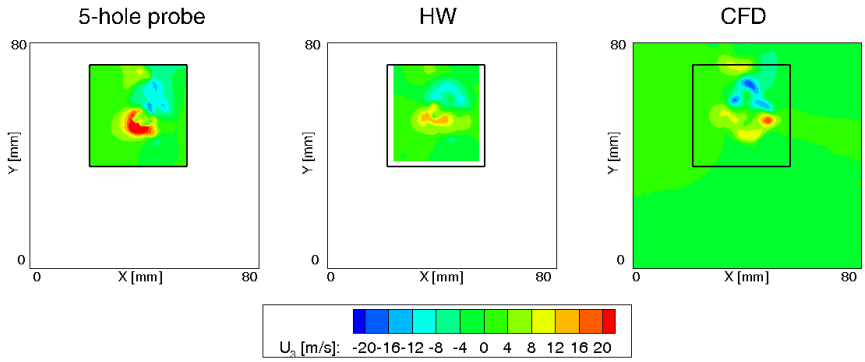

Figure 7: Tangential velocity contours at first traversing plane.

is swirled mainly by channels 3-4-5, as indicated by the streamlines of the injected streak shown in Fig. 6. Being the first measuring plane approximately 10 mm downstream of the swirler generator, the flow structures are not yet completely mixed, thus justifying the presence of velocity peaks. While both probes record the three regions labelled 3-4-5, a lower velocity peak is measured, underlying that the main issue of RANS is to correctly predict the mixing process.

For the same reasons, the tangential velocity contours (Fig. 7) show the lowest absolute magnitudes on the left part of the swirl profile, corresponding to swirler generator channels 1-2. The differences between simulations and experiments are mainly quantitative, as the trends are very similar. Both in simulations and experiments, a reduction of high positive/negative tangential velocities is observed during the circumferential evolution, which is caused by the wakes of the swirler generator blades.

The agreement between HW and CFD in terms of turbulence intensity is good (Fig. 8), which is defined as the ratio of the root-mean-square of the turbulent velocity fluctuations and the mean velocity. The area average value on the measuring grid in CFD is 7.2 % against the 6.1 % measured experimentally. These values match the turbulence intensity found by Pinelli et al. (2023) in their CFD study. Turbulence is generated downstream of the combustor simulator in the regions of the injector stem wake and swirl core. The region with the highest turbulence intensity is the injector stem wake, very well predicted by CFD. In the swirling flow zone, some points of the HW grid are not fully converged because the HW works close to its angular calibration limits. Despite this, turbulence intensity levels in the swirl core match well between simulation and experiment. However, CFD predicts high turbulence in an annular zone contouring the swirl core, that is generated by the shear layer formed at the boundary between the flow released by the swirler generator and the free-stream. This feature is not measured in experiments, probably due to the mixing that takes place and nullifies this contribution, that is underestimated in CFD. In both CFD and HW measurements, the high velocity zones (3-4-5 Fig. 5) have low turbulence levels. Therefore, the main contribution to

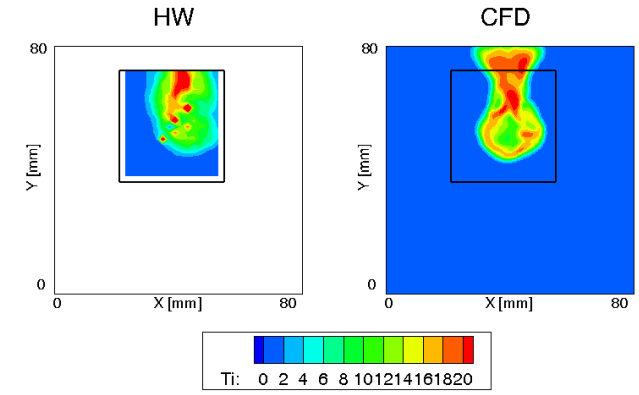

Figure 8: Turbulence intensity contours at first traversing plane.

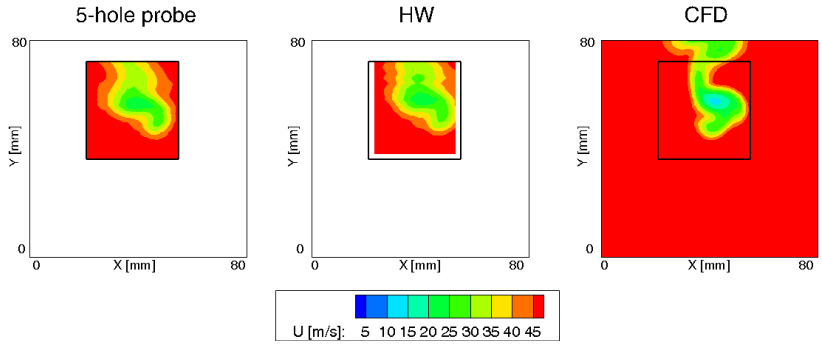

Figure 9: Absolute velocity contours at Plane 2.

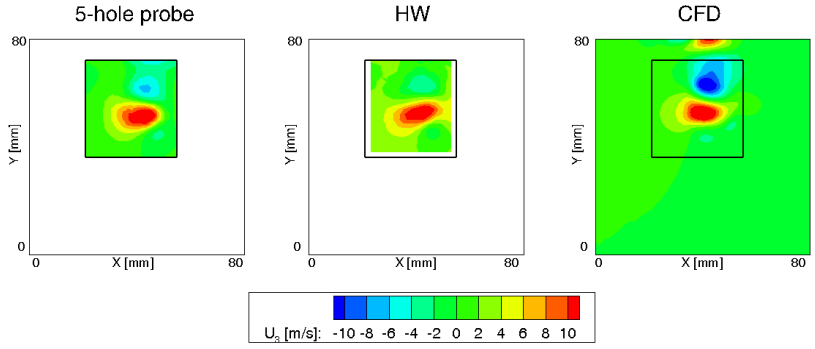

Figure 10: Tangential velocity contours at Plane 2.

turbulence production in this measuring traverse is related to the boundary layers of the injector walls.

At the second traversing plane, the flow structures are dominated by the interaction between the swirl profile and the flows identified as 4 and 5 in Fig. 5. These two high-momentum flows break the pattern of the swirl profile, elongating it in the X-axis direction and generating a "tail" at the bottom of the swirl profile (Fig. 9). This structure is well predicted by the CFD and only differs from the experiments in its X-axis position. The flow regions 4 and 5 are dominated by the cold streak and possible differences in the injector manufacturing could change the CS/swirler generator interaction, making its simulation less reliable. CFD shows a lower velocity in the swirling flow core than experiments, possibly due to an underestimation of the mixing.

The tangential velocity contours (Fig. 10) show that the shear interaction between the swirl profile and the boundary layer on the outer casing of the swirler generator results in a counter-rotating vortex in the bottom-right part of the swirl profile.

Simulations slightly overestimate the turbulence intensity (Fig. 11) with an area-average value of 6.6 % compared to the experimental value of 5.9 %, even though the wake is thinner. CFD foresees a similar turbulence intensity at the swirl core as the hot-wire results and an increased Ti in an annular region contouring the center of the vortex due to the shear interaction between the regions 3-4-5 and the surrounding fluid, while zones 1-2 are completely mixed.

The turbulence intensity is area-averaged at different axial positions to study its decay and it is shown in Fig. 12. This plot is compared to a cross-section of the calculation domain along the Y-axis which shows that there are four main mechanisms producing turbulence due to the shear flows interaction. These include the injector stem wake, the boundary layer developing around the outer casing of the swirler generator, the generation of the swirl profile and the injection of the streak inside the injector. Along the axial direction, five different regions of turbulence decay can be identified and numbered in Fig. 12. In the 1st region, turbulence is strongly generated by the four aforementioned

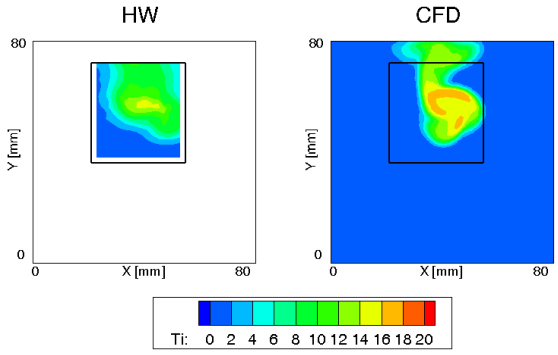

Figure 11: Turbulence intensity contours at Plane 2.

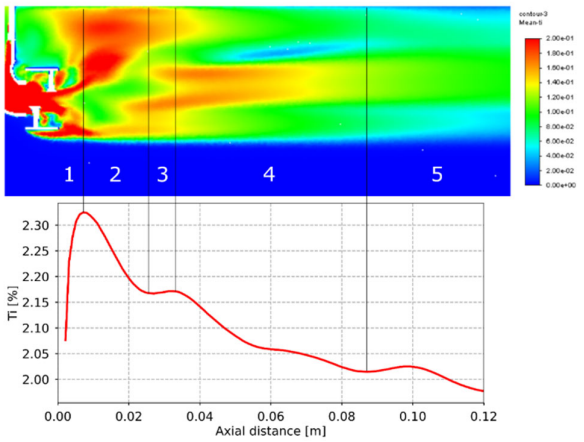

Figure 12: Turbulence intensity decay.

mechanisms. In the 2nd region, the injector stem wake and the boundary layer around the swirler generator casing start decaying, while the swirler core still generates turbulence. Overall, the trend is a reduction of the turbulence intensity. In the 3rd region, the turbulence production in the swirl region compensates for the decay in the other regions, leading to a slight increase in turbulence levels. In the 4th region, the turbulence starts decaying also in the swirl region, notwithstanding some shear interactions between the different zones are still present, altering the decay rate. Finally, in the 5th region, the wake of the injector stem rejoins the swirling zone, producing new turbulence that then begins to decay again.

A further analysis regards the decay of the swirl number (SN), defined accordingly to Eq. 15.

$$SN = \frac{\int r U_\Theta \left(\vec{U} \cdot \hat{n}\right) dS}{\bar{r} \int U_z \left(\vec{U} \cdot \hat{n}\right) dS} \tag{14}$$

$\vec{U}$ is the velocity vector, S the surface of integration, r the radial coordinate, $\bar{r} = 1/S \int r dS$, $\hat{n}$ the unit vector perpendicular to the surface, z is the axial coordinate and Θ the tangential one of a cylindrical reference system centered in the vortex center. The SN is computed on the surface of the measuring grid of the 5-hole probe, and measurements obtained from it are shown as filled circles in Fig. 13. The center of the cylindrical reference system is taken at the coordinates of the swirler generator center. The agreement is good between calculations and measurements in Fig. 13. The swirl profile is almost fully developed at an axial distance of approximately one swirler generator blade chord, which corresponds closely to the location of the first measuring point. The swirl profile stabilizes and starts decaying after approximately two swirler generator blade chords. The decay follows a power law obtained by a least square regression on the CFD data (Eq. 15).

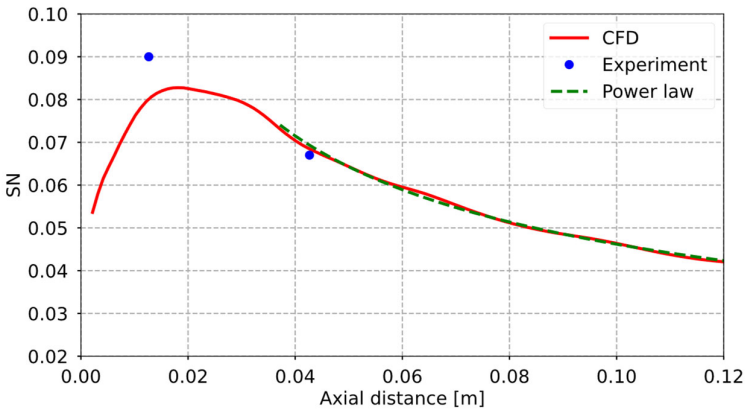

Figure 13: Swirl number decay.

$$SN = 0.0154 z^{-0.477} \tag{15}$$

Furthermore, the calculated SN over the region of the swirl profile is 0.61, that is consistent with

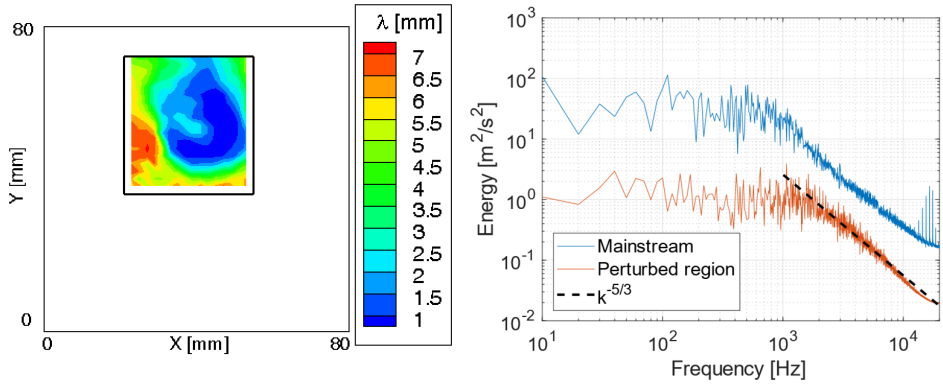

Figure 14: integral length scale (left) and energy spectrum (right) at plane 1.

the value measured upstream of the turbine in the turbine test rig (Notaristefano and Gaetani (2023a)).

To enable the setup of high-fidelity CFD simulations on the turbine test section, the turbulence length scales are crucial parameters. For this purpose, the Roach (1987) method has been used to compute the integral length scale. Specifically, the integral length scale is determined by integrating the autocorrelation of the velocity from zero up to the first crossing of the autocorrelation to 1/e. This effectively eliminates any random noise that may cause a delay in the crossing of zero. The velocity signal used is associated with the hot-wire rotation closest to the actual flow angle. The results of the integral length scale are shown in Fig. 14. The highest values are around the wake region and in the mainstream flow, the lowest in the core of the wake. This is consistent with the low velocities in the region of injector stem wake and swirl profile that reduce the turbulent kinetic energy content. In the Fig. 14 right plot, two dimensional energy spectra are shown, computed as the Fourier transform of the velocity autocorrelation (Kundu et al. (2012)). The plot shows results from two different grid points: one sampled from the mainstream zone (labeled 'Mainstream' in the legend), and another obtained from the swirl profile (labeled 'Perturbed region'). The spectra clearly show an inertial region following the -5/3 power law. The energy associated with the point in the perturbed region has lower turbulent kinetic energy due to the lower velocity than the mainstream one. This analysis indicates that a nearly isotropic turbulence is generated by the combustor simulator.

Unsteady cold streaks at 110 Hz

To study the evolution during the EW period, the analysis of the unsteady injection case compares CFD results with HW measurements. To this end, the HW data are post-processed by first identifying the EW periods using the trigger pressure signal, and then dividing each EW period into 20 intervals. The number of intervals was chosen so to obtain converged statistics. Then, given a number of samples of 40000, an acquisition frequency of 40000 Hz and the EW frequency of 110 Hz, each interval has approximately 18 samples. However, 18 samples are not enough to guarantee a good statistic to compute E and e. Therefore, considering the periodicity of the phenomena and its good repeatability, the proposed procedure analyzes more than 1 period, specifically all those included in 1 second of data acquisition. In such a way, a voltage supply array of 2000 points is generated for each interval, considered sufficient to ensure reliable statistical analysis. The computed $\boldsymbol{E}$ and $\boldsymbol{e}$ are used to solve the HW over-constrained problem for each interval. The main drawback of this procedure is the reduction of the highest frequency that can be encoded from 20000 Hz to 1100 Hz, according to the Nyquist limit. Nonetheless, this frequency range is well above the range of interest. The results of this analysis are compared with CFD in terms of turbulence intensity in Fig. 15 and 16 highlighting only 6 phases that correspond to 0-15-30-45-60-80% of the EW period. In the HW case, these phases are selected from the 20 snapshots generated through the aforementioned procedure at the chosen timing.

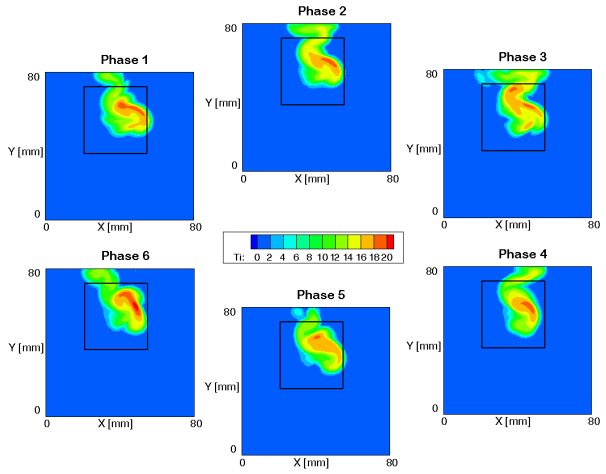

Figure 15: CFD turbulence intensity snapshots at Plane 2.

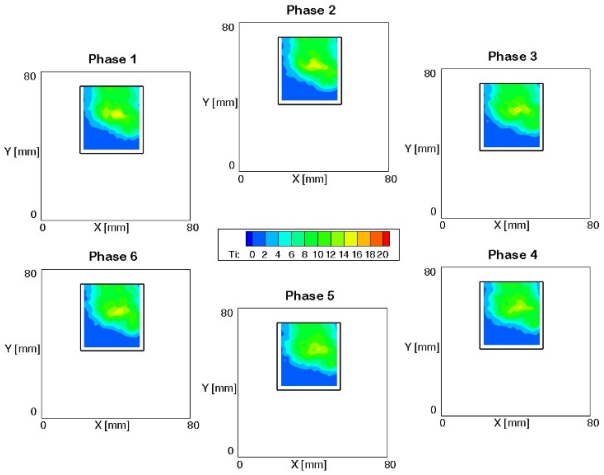

Figure 16: HW turbulence intensity snapshots at Plane 2

Table 4: SN at Plane 2 time evolution

		CFD	HW
Streak 1	Phase 1	0.087	0.088
	Phase 2	0.084	0.088
	Phase 3	0.096	0.092
Streak 2	Phase 4	0.101	0.094
	Phase 5	0.108	0.093
	Phase 6	0.114	0.092

The CFD outcomes are plotted at each time-instant, while the HW results are derived through the discussed procedure that involves averaging, thus reducing the available frequency content. For this reason, CFD data experiences a significant time-dependence, not fully captured by the HW. The unsteadiness in the CFD is due to the vortex shedding in the wake of the injector stem, which cannot be revealed by measurements due to the aforementioned issues, and to the alternative feeding of the ducts 1 and 2 (Fig. 1). Each of these two streams interacts differently with the swirler generator changing the generation of the swirl profile. The streak 1 is more dissipated inside the injector, since it has to significantly turn inside the device. The streak 2 follows the shape of the injector and it exhibits a lower mixing. As a result, the turbulence intensity is higher during the injection period of duct 1 (phases 1-3) than in the one corresponding to duct 2 (phases 4-6). For the same reason, the SN calculated in each of the times steps in the HW measuring grid is higher during the streak 2 period than the streak 1 in both CFD and HW measurements (Tab. 4). Both methodologies predict a more compacted shape of the combustor-representative disturbance in phases 4-6 than 1-3. The reason is that the streak 1 and streak 2 interact differently with the swirler generator and the tail generation identified in the bottom part in Fig. 9 is less intense during the injection of duct 2 than 1.

Temperature effect

Turbulence intensity is not significantly affected by the temperature, underlying the reliability of carrying out experiments without heating the streak flowing in duct 1. Being cross-flows and shear interactions the main drivers of turbulence generation, temperature could modify these phenomena impacting the cinematic viscosity. At the two measuring planes, results are listed in Tab. 5 as area-average on the HW measuring grid in terms of SN and turbulence intensity. CFD results are time-averaged over one EW period, whereas HW experimental results are averaged over the entire acquisition period. The injection of a heated jet does not impact significantly the results, despite the small temperature increase imposed on the main flow. Although the air temperature at the combustor simulator exit increases at approximately 400 K, it is unlikely to significantly affect the turbulent diffusion.

As a result of the temperature increase, the flow is faster due to a density effect and this increases

the turbulence generation due to the shear interaction. The aerodynamics is not significantly modified and the SN is approximately unchanged.

A final consideration can be drawn comparing steady and unsteady cases: if the mean value of the unsteady cases is considered, these values are very close to the steady cases, confirming that EW can be treated as a series of HS, as previously found and discussed in Gaetani and Persico (2019).

Table 5: SN and area-average Ti for the different injection cases.

		SN				Ti			
		Unsteady CS	EW	CS	HS	Unsteady CS	EW	CS	HS
Plane 1	Exp	0.12		0.09		6.5%		6.1%	
	CFD	0.12	0.11	0.10	0.10	7.2%	7.3%	7.2%	7.4%
Plane 2	Exp	0.09		0.09		5.9%		5.9%	
	CFD	0.09	0.08	0.08	0.08	6.4%	6.4%	6.4%	6.9%

CONCLUSIONS

In this paper, the flow field generated by a combustor simulator is studied by means of experiments and RANS CFD computations. The main purpose of the investigation is to evaluate the turbulence intensity produced by the combustor simulator used in the combustor-turbine interaction experiments carried out on the Politecnico di Milano turbine test rig.

The results indicate that at the plane representing the turbine vane LE (plane 2), the turbulence intensity locally increases from 1% in the mainstream region to 10-16% in the regions of the injector stem wake and swirl profile, due to the presence of the combustor simulator. In the literature, similar values of the turbulence intensity are reported, emphasizing the capability of this device to simulate all the features of a real combustor. The agreement between CFD and experiments is good, showing that the use of RANS-based simulation models is suitable for this kind of analyses, even though higher fidelity methods such as LES might also be considered. As a matter of fact, considering the proximity of the two measuring planes to the combustor simulator, RANS is still in a region where the turbulence model provides satisfactory results.

The detailed information on turbulence properties achieved in this work will be crucial to support high-fidelity CFD simulations, to deepen the knowledge of the flow and turbulent processes measured in the frame of combustor-turbine interaction experiments.

REFERENCES

Adams, M. G., Beard, P. F., Stokes, M. R., Wallin, F., Chana, K. S., and Povey, T., (2021). *Effects of a combined hot-streak and swirl profile on cooled 1.5-stage turbine aerodynamics: an experimental and computational study*. ASME. J. Turbomach., 143(2): 021011.

Andreini, A., Bacci, T., Insinna, M., Mazzei, L., and Salvadori, S., (2016). *Hybrid RANS-LES modeling of the aerothermal field in an annular hot streak generator for the study of combustor–turbine interaction*. ASME. J. Eng. Gas Turbines Power, 139(2).

Bacci, T., Facchini, B., Picchi, A., Tarchi, L., Koupper, C., and Champion, J., (2015). *Turbulence Field Measurements at the Exit of a Combustor Simulator Dedicated to Hot Streaks Generation*. Proceedings of the ASME Turbo Expo 2015, Montreal, Quebec, Canada.

Bons, J. P., (2002). *St and cf augmentation for real turbine roughness with elevated freestream turbulence*. ASME. J. Turbomach., 124, pp.623–644.

Bruun, H. H., (1995). *Hot-Wire Anemometry*. Oxford Univ. Press, New York.

Buresti, G., and Di Cocco, N. R., (1987). *Hot-wire measurement procedures and their appraisal through a simulation technique*. J. Phys. E: Sci. Instrum., 20(1):87-99.

Cha, C. M., Hong, S., Ireland, P. T., Denman, P., and Savarianandam, V., (2012). *Turbulence levels are high at the combustor-turbine interface.* Proceedings of the ASME Turbo Expo 2012, Copenhagen, Denmark.

Cresci, I., Ireland, P.T., Bacic, M., Tibbott, I., and Rawlinson, A., (2015). *Realistic velocity and turbulence intensity profiles at the combustor-turbine interaction (CTI) plane in a nozzle guide vane test facility*. Proceedings of 11th European Conference on Turbomachinery Fluid dynamics & Thermodynamics ETC11, Madrid, Spain.

Fitouri, A., Khan, M.K., Bruun, H.H., (1995). *A multiposition hot-wire technique for the study of swirling flows in vortex chambers.* Exp. Therm. Fluid Sci., 10(1):142-151.Folk, M., and Miller, R. J. (2019). *Design and Test of a Combustor Simulator*. AIAA 2019-4256. AIAA Propulsion and Energy 2019 Forum.

Folk, M., Miller, R. J., and Coull, J. D., (2020). *The Impact of Combustor Turbulence on Turbine Loss Mechanisms*. ASME. J. Turbomach, 142(9): 091009.

Gaetani, P., and Persico, G. (2019). *Transport of Entropy Waves Within a High Pressure Turbine Stage*. ASME. J. Turbomach., 141(3): 031006.

Gundy-Burlet, K. L., and Dorney, D. J., (1997). *Influence of 3d hot streaks on turbine heat transfer*. Proceedings of the ASME Turbo Expo 1997, Orlando, Florida, USA.

Khanal, B., He, L., Northall, J., and Adami, P., (2013). *Analysis of radial migration of hot-streak in swirling flow through high-pressure turbine stage*. ASME. J. Turbomach., 135(4): 041005.

Kundu P.K., Cohen I.M., and Dowling, D.R. (2012). *Fluid Mechanics.* Elsevier Science

Mansouri, Z., and Jefferson-Loveday, R., (2022). *Heat transfer characteristics of a high-pressure turbine under combined distorted hot-streak and residual swirl: an unsteady computational study.* Int. J. Heat Mass Transf., 195.

Morgans, A. S., and Duran, I., (2016). *Entropy noise: A review of theory, progress and challenges*. Int. J. Spray Combust. Dyn., 8(4).

Notaristefano, A., and Gaetani, P., (2020). *Design and Commissioning of a Combustor Simulator Combining Swirl and Entropy Wave Generation*. Int. J. Turbomach. Propuls. Power, 5, 27.

Notaristefano, A., Gaetani, P., Dossena, V., and Fusetti, A., 2021. *Uncertainty Evaluation on Multi-Hole Aerodynamic Pressure Probes.* ASME. J. Turbomach., 143(9): 091001.

Notaristefano, A., and Gaetani, P., (2023). *The Role of Turbine Operating Conditions on Combustor–Turbine Interaction—Part I: Change in Expansion Ratio.* ASME. J. Turbomach., 145(5): 051001.

Notaristefano, A., and Gaetani, P. (2023). *The Role of Turbine Operating Conditions on Combustor–Turbine Interaction—Part II: Loading Effects*. ASME. *J. Turbomach*., 145(5): 051002.

Perdichizzi, A., Ubaldi, M., and Zunino, P., (1990). *A hot wire measuring technique for mean velcity and Reynolds stress components in compressible flow*. Proceedings of the X Biannual Symposium on Measuring Techniques in Turbomachinery, Sint-Genesius-Rode, Belgium.

Persico, G., Dossena, V., and Gaetani, P., (2010). *On the capability of fast response total pressure probes to measure turbulent kinetic energy.* Proceedings of the XX Biannual Symposium on Measuring Techniques in Turbomachinery, Milano, Italy.

Pinelli, L., Marconcini, M., Pacciani, R., Notaristefano, A., and Gaetani, P., (2023). *The Effects of Swirling Flows in Entropy Wave Convection Through High-Pressure Turbine Stage*. ASME. J. Turbomach., 145(3): 031004.

Rahim, A., and He, L., (2015). *Rotor blade heat transfer of high pressure turbine stage under inlet hot-streak and swirl*. ASME. J. Eng. Gas Turbines Power, 137(6).

Roach P.E., (1987). The generation of nearly isotropic turbulence by means of grids. Int. J. Heat Fluid Flow, 8(2), 82-92.

Werschnik, H., Schneider, M., Herrmann, J., Ivanov, D., Schiffer, H.P., Lyko, C, (2017). *The Influence of Combustor Swirl on Pressure Losses and the Propagation of Coolant Flows at the Large Scale Turbine Rig (LSTR): Experimental and Numerical Investigation*. Int. J. Turbomach. Propuls. Power., 2(3):12.

Seasholtz, R. G., Oberle, L. G., and Weikle D. H., (1983). *Laser anemometry for hot section applications.* NASA CP-2289.

Thole K. A., and Bogard D. G., (1995). *Enhanced heat transfer and shear stress due to high free-stream turbulence.* ASME. J. Turbomach., 117(3):418-424.

Zimmerman, D. R., (1979). Laser anemometer measurements at the exit of a T63-C20 combustor. NASA CR-159623.

